Journal of Colloid and Interface Science 578 (2020) 171–183

Contents lists available at ScienceDirect

Journal of Colloid and Interface Science

journal homepage: www.elsevier.com/locate/jcis

Covalently and ionically, dually crosslinked chitosan nanoparticles block quorum sensing and affect bacterial cell growth on a cell-density dependent manner

C. Vila-Sanjurjo [a,b,1], L. Hembach [a,b,1], J. Netzer [a], C. Remuñán-López [b], A. Vila-Sanjurjo [c,*], F.M. Goycoolea [a,d,*]

[a] Westfälische Wilhelms Universität Münster. IBBP, Laboratory of Nanobiotechnology, Schlossplatz 8, Münster 48143, Germany
[b] Nanobiofar Group. Department of Pharmacology, Pharmacy and Pharmaceutical Technology, Universidade de Santiago de Compostela, Campus Vida, s/n, 15782 Santiago de Compostela, Spain
[c] Grupo GIBE. Departamento de Bioloxía e Centro de Investigacions Científicas Avanzadas (CICA), Universidade da Coruña (UDC). Campus Zapateira, s/n, 15071 A Coruña, Spain
[d] School of Food Science and Nutrition. University of Leeds, Leeds LS2 9JT, United Kingdom

GRAPHICAL ABSTRACT

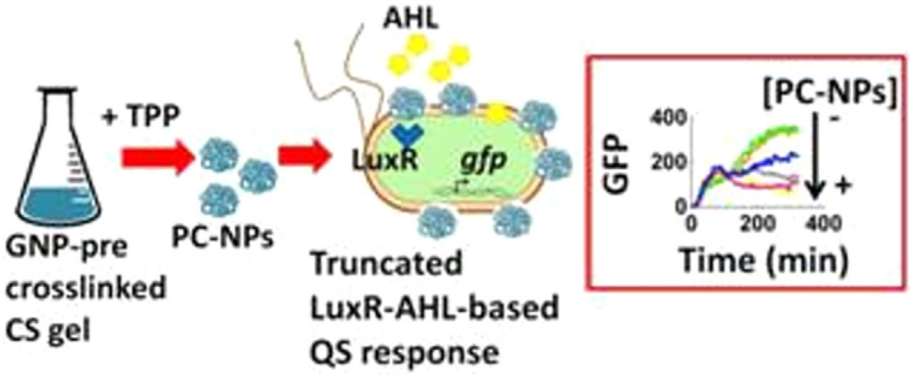

ARTICLE INFO

Article history:
Received 13 April 2020
Revised 16 May 2020
Accepted 18 May 2020
Available online 24 May 2020

ABSTRACT

In our efforts to improve the quality and stability of chitosan nanoparticles (NPs), we describe here a new type of chitosan NPs dually crosslinked with genipin and sodium tripolyphosphate (TPP) that display quorum quenching activity. These NPs were created using a simplified and robust procedure that resulted in improved physicochemical properties and enhanced stability. This procedure involves the covalent crosslinking of chitosan with genipin, followed by the formation of chitosan NPs by ionic gelation with TPP. We have optimized the conditions to obtain genipin *p*re-*c*rosslinked *n*anoparticles (PC-NPs) with

Abbreviations: AHL, acyl homoserine lactone; AUC, area under the curve; CC-NPs, genipin-*c*o-crosslinked chitosan nanoparticles; CLSM, confocal laser scanning microscopy; CS, chitosan; CS NCs, CS-based nanocapsules; DA, degree of acetylation; DLS-NIBS, dynamic light scattering with non-invasive back scattering; FI, fluorescence intensity; FI/OD_{600}, density-normalized fluorescence intensity; FTIR, Fourier transform infrared spectroscopy; *G'*, elastic modulus; *G''*, viscous modulus; GFP, green fluorescent protein; GNP, genipin; γ, strain; η^*, complex viscosity; IC-NPs, ionically crosslinked chitosan nanoparticles; PD, polymer polydispersity index; M3-PALS, phase analysis light scattering with mixed mode measurements; *Mn*, number-average molecular weight; *Mw*, weight-average molecular weight; NMR, nuclear magnetic resonance; NPs, nanoparticles; OD_{600}, bacterial optical density; PC-A, PC-NP prototype A; PC-B, PC-NP prototype B; PdI, particle polydispersity index; PC-NPs, GNP-pre-crosslinked CS-TPP NPs; NCs, nanocapsules; PT, Percolation Theory; QQ, quorum quenching; QS, quorum sensing; ROIs, regions of interest; SR, stoichiometric ratio; tan_δ, liquid-like character; $t_{gel\text{-}DLS}$, critical gel time obtained by DLS-NIBS; TPP, sodium tripolyphosphate; $t_{gel\text{-}rheo}$, rheological critical gel time; ω, oscillation frequency.

* Corresponding authors at: School of Food Science and Nutrition. University of Leeds, Leeds LS2 9JT, United Kingdom (F.M. Goycoolea); Departamento de Bioloxía e Centro de Investigacions Científicas Avanzadas (CICA), Universidade da Coruña (UDC). Campus Zapateira, s/n, 15071 A Coruña, Spain (A. Vila-Sanjurjo).
E-mail addresses: anton.vila@udc.es (A. Vila-Sanjurjo), F.M.Goycoolea@leeds.ac.uk (F.M. Goycoolea).
[1] Present affiliation: Nanobiofar Group. Department of Pharmacology, Pharmacy and Pharmaceutical Technology, Universidade de Santiago de Compostela, Campus Vida, s/n, 15782 Santiago de Compostela, Spain.

https://doi.org/10.1016/j.jcis.2020.05.075

Keywords:
Chitosan
Nanoparticles
Quorum sensing
Bacteria
Genipin
Percolation theory

positive ς-potential (~ +30 mV), small diameter (~130 nm), and low size distributions (PdI = 0.1–0.2). PC-NPs present physicochemical properties that are comparable to those of other dually crosslinked chitosan NPs fabricated with different protocols. In contrast to previously characterized NPs, however, we found that PC-NPs strongly reduce the acyl homoserine lactone (AHL)-mediated quorum sensing response of an *Escherichia coli* fluorescent biosensor. Thus, PC-NPs combine, in a single design, the stability of dually crosslinked chitosan NPs and the quorum quenching activity of ionically crosslinked NPs. Similar to other chitosan NPs, the mode of action of PC-NPs is consistent with the existence of a "stoichiometric ratio" of NP/bacterium, at which the positive charge of the NPs counteracts the negative ς-potential of the bacterial envelope. Notably, we found that the time of the establishment of the "stoichiometric ratio" is a function of the NP concentration, implying that these NPs could be ideal for applications aiming to target of bacterial populations at specific cell densities. We are confident that our PC-NPs are up-and-coming candidates for the design of efficient anti-quorum sensing and a new generation antimicrobial strategies.

1. Introduction

Chitosan (CS) is a family of cationic and biodegradable aminopolysaccharide polymers derived from partial deacetylation of chitin. The physical and chemical properties of CS are mainly determined by the relative abundance of deacetylated units and by their molecular weight. This versatility makes CS a strong candidate for applications in the food, cosmetic, pharmaceutical and biomedical fields [1]. Physical or chemical crosslinking is frequently applied to improve the physicochemical properties of CS towards the design of efficient CS-based biopharmaceuticals [2–4]. Ionic crosslinking normally involves polyanions, such as sodium tripolyphosphate (TPP), which interact with the protonated amine-groups of CS [5–9]. Chemical crosslinking of CS has been reported to increase its stability against pH, temperature, and degradation, both biological and mechanical [3–4,10–12]. Genipin (GNP) is a natural covalent crosslinker derived from the geniposide compound found in the fruits of *Gardenia spp*. GNP is receiving intense attention as it constitutes a more compatible and less cytotoxic alternative to covalent crosslinkers such as glutaraldehyde [13–16]. The crosslinking reaction between GNP and CS occurs in two steps. First, a nucleophilic attack of a CS primary amine group to the GNP C3 carbon atom leads to the formation of a heterocyclic compound linked to a glucosamine residue. This reaction is followed by a slower nucleophilic substitution of the GNP ester group (C11), the formation of a secondary amide linkage with CS, and the formation of crosslinking bridges [15]. The degree of covalent crosslinking with GNP can be controlled to modulate specific properties of CS-based materials, such as the release of biomolecules, the stability against pH and temperature variations, or the structure of the CS gel network. Due to all these properties, GNP-based crosslinking of CS is the subject of an increasing number of applications in the fields of Material Sciences, Biotechnology and Pharmaceutical Technology [11,13,17–21].

Quorum sensing (QS) is a cell-to-cell signaling mechanism mediated by exocellular chemical compounds that act as autoinducers. QS is reported to control many bacterial phenotypes, from bioluminescence to antibiotic production, biofilm formation, and secretion of virulence factors, among others [22–25]. In Gram-negative bacteria, the molecular family of the acyl-homoserine lactones (AHLs) constitute the most abundant species of autoinducers [26,27]. AHLs are synthesized by LuxI-type enzymes and can freely diffuse in and out of the cell, where they bind to LuxR-type regulators of QS gene expression [28–29]. Since QS is deeply involved in the development of pathogenicity in bacteria, the search for anti-QS strategies, or quorum quenching (QQ), is a growing field of interest. QQ strategies typically include the use of agents capable of blocking QS molecular mechanisms. As such, QQ can occur by the inactivation of either the autoinducer, its receptor, or the AHL synthase [23,30–37]. Research on the potential use of CS to interfere with QS has been gaining traction [11,38–41].

In a recent paper [42], we reported the ability of ionically crosslinked CS nanoparticles (NPs) using TPP (IC-NPs), to interfere with QS. Despite their QQ activity, IC-NPs displayed high polydispersity and low colloidal stability in microbiological medium. As a first attempt to overcome this, we crosslinked IC-NPs with GNP and found that this treatment led to the formation of a core–shell ultrastructure that stabilized the system, albeit with a significant decrease of their QQ activity [42]. While the resulting NPs, hereafter named CC-NPs, were potentially useful in contexts in which QQ is not desired, we set out to find new formulations that combined the stability of CC-NPs with the QQ activity of IC-NPs. In the present work, we found that by reversing the preparation protocol to first crosslinking of CS with GNP close to the critical gelling condition, followed by ionotropic formation of NPs in the presence of TPP, resulted in NPs displaying improved physico-chemical features while retaining the QQ and antimicrobial activity. This, along with the fact that the uncovered fabrication process is faster and more robust, made us confident that these NPs could serve as the chassis for the development of CS-based nanomaterials intended for microbiological applications. We named these GNP *p*re-crosslinked *NP*s (PC-NPs). Besides, we show here that PC-NPs have the potential to target bacterial populations in a cell-density specific manner. This feature could be used for the targeting of bacterial populations at specific stages of growth.

2. Experimental section

2.1. Materials

High-purity grade CS in its hydrochloride salt form (Protasan UP CL113) was purchased from Novamatrix (FMC-Biopolymer, Norway). Chitosan *Mw* was ~ 92 kDa, *PD (Mw/Mn)* ~ 2.5, as determined by GPC-MALLS-DRI; and the degree of acetylation (DA) was ~ 14%, as determined by ^{1}H NMR. GNP was purchased from Challenge Bioproducts Co. Ltd. (Touliu, Taiwan). TPP, N-(3-oxo-hexanoyl)-L-homoserine lactone (3OC6HSL, named AHL hereafter), and other chemicals were purchased from Merck KGaA, (Darmstadt, Germany). Milli-Q water was used throughout. All reagents were of analytical grade.

2.2. Chemical pre-crosslinking of CS with GNP

Before the preparation of the mixtures of CS and GNP (CS/GNP), stock solutions of CS (2 mg/mL) and GNP (5 mg/mL), were prepared directly in 85 mM NaCl, sterile-filtered through a 0.22-μm membrane, and stored at 4 °C until use. CS hydrochloride salt dissolves directly in water [43]. To assess the optimal composition and con-

sistency of the CS/GNP mixture, we screened different GNP:CS mass ratios. To this end, working solutions of CS (2 mg/mL) and GNP (0.12, 0.24 and 0.48 mg/mL) were first prepared in 85 mM NaCl. Next, aliquots of the two components were mixed in a final volume of 30 mL to obtain CS/GNP mixtures with 0.06:1, 0.12:1 and 0.24:1 GNP:CS mass ratios. The mixtures were incubated for 72 h in capped, 100-mL Erlenmeyer flasks at 37 °C in an orbital shaker (100 rpm).

The kinetics of the crosslinking reaction was monitored by UV/VIS spectroscopy (V-630 UV–VIS Spectrophotometer, JASCO Corporation, Tokyo, Japan) (λ = 200–900 nm) and by dynamic light scattering using non-invasive back scattering (DLS-NIBS) with a Malvern Zetasizer NanoZS ZEN 3600, (Malvern Panalytical, UK); equipped with a red 4mW He/Ne laser output operating at λ = 63 3 nm. In both cases, one mL-aliquots of the CS/GNP mixtures were transferred to measurement cuvettes at specific time points, spanning a total of 72 h of sample incubation. The samples were measured in triplicates, and each one of them was measured three times at 37 °C. After each measurement, the aliquots were returned to the batch solution.

To estimate the critical gel time, the DLS-NIBS intensity correlation data were approximated by percolation kinetics [44]. First, the intensity correlation function $g^{(2)}(t_D)$-1 was fitted to the modified exponential stretched KWW function, as explained in de Morais *et al.* [45]. Thus, the initial part of the DLS correlograms, expressed as the correlation coefficients *vs*. delay times (t_D), was fitted to the KWW-based stretched exponential equation (Equation (1)) with Origin Pro 8 (OriginLab, Northampton, MA):

$$g^{(2)}(t_D) - 1 = 1 - \beta e^{-(2\Gamma_c t_D)} \quad (1)$$

where β is a constant that depends on the optical properties of the system, and Γ_c is the relaxation rate [45].

The estimated Γ_c values were then corrected by subtracting the baseline, plotted against incubation time, and fitted to the percolation scaling law function (Equation (2)).

$$P_\infty = K(p - p_c)^M \quad (2)$$

This equation is equivalent to the three-parameter power Belehradek function (OriginLab, Northampton, MA), where P_∞ is the calculated evolution of the correlation coefficient Γ_c over time, K is a proportionality constant, p is time, M is the universal percolation exponent, and p_c becomes $t_{gel\text{-}DLS}$, *i.e.* the critical gelation time at which the response diverges from that in the sol state [46]. The use of the Belehradek function to approximate percolation phenomena has been described [47–49].

The evolution of the viscoelastic properties for the CS:GNP mix (ratio 0.06:1) was further examined by small deformation oscillatory rheology using a stress-controlled rheometer Kinexus Ultra (Malvern Panalytical Ltd, UK) fitted with a truncated cone and plate geometry (gap 0.07 mm; diameter 50 mm). To this end, the CS/GNP mixture was prepared by mixing the corresponding amounts of CS and GNP stock solutions in a glass vial and incubated at 37 °C in quiescent conditions during 18 h. A 1.5 mL aliquot of the mixture was loaded to the plate of the rheometer and the rim of the cone was covered with low viscosity silicon oil to avoid evaporation. The critical rheological gel point was defined as the crossover point of the elastic (G') and viscous (G'') moduli (ω = 6. 28 rad/s), recorded at strain values, γ = 1% over a period of up to 106 min), in line with previous studies [50–51].

2.3. Preparation of PC-NPs

The GNP-pre-crosslinked CS-TPP NPs (PC-NPs) were prepared according to the general ionotropic gelation protocol described by Calvo *et al.* [6] with some modifications. First, GNP-pre-crosslinked CS was prepared at a GNP:CS mass ratio of 0.06:1, as explained above. To assess the optimal formulation to obtain PC-NPs of an average size ~ 200 nm and low polydispersity index or PdI (PdI ~ 0.1), different CS:TPP mass ratios were screened. To do this, GNP-pre-crosslinked CS was sub-diluted with 85 mM NaCl to reach CS concentrations ranging from 1 to 2 mg/mL. Similarly, TPP was also prepared in 85 mM NaCl, achieving final concentrations ranging from 0.5 to 0.83 mg/mL. Aliquots of the two components were mixed in a 96-well microplate to obtain PC-NPs with CS:TPP mass ratios ranging from 1.60:1 to 9.00:1 (see Table S1).

Two PC-NP prototypes of optimal size and PdI, namely PC-A, PC-B, with CS:TPP mass ratios of 3.5:1 and 2.6:1, respectively, were prepared by upscaling the preparation technique. Briefly, 1.875 mL (PC-A) or 2.250 mL (PC-B) of a TPP solution (0.63 mg/mL in 85 mM NaCl) were poured onto 4.125 mL (PC-A) or 3.750 mL (PC-B) of GNP-pre-crosslinked CS (sub-diluted to a CS concentration of 1 mg/mL with 85 mM NaCl) under magnetic stirring (500 rpm). When necessary, PC-NPs were isolated by centrifugation (40 min at 10000 × g and at 25 °C) in 1.5 mL vials containing a glycerol bed [52] and the pellets were re-suspended in 100 μL of water.

2.4. Physicochemical characterization of PC-NPs

The size distribution of NPs re-suspended in Milli-Q® water was determined by DLS-NIBS in Milli-Q® water (pH ≈ 7.0) at 25.0 ± 0. 2 °C. The ς-potential was determined by phase analysis light scattering with mixed mode measurements (M3-PALS) in the same instrument as for DLS-NIBS measurements, and diluting (1:50) the PC-NPs in 1 mM KCl (pH 5.89).

2.5. Determination of the PC-NP production yield and concentration

Batch PC-NP production yield was determined by centrifugation (40 min at 10000 × g and at 25 °C) of fixed volumes of freshly prepared PC-NPs in the absence of glycerol. After discarding the supernatants, the pellets were subjected to freeze-drying and the dry weight of the pellets was registered. The production yield was determined as follows (Equation (3)):

$$Production\ yield\ (\%) = 100 \times \frac{m_{pellet} - m_{NaCl(pellet)}}{m_{total} \times V} \quad (3)$$

where: m_{pellet} is the dried mass of the pellet, m_{NaCl} *(pellet)* is a corrective term that accounts for the mass of the residual NaCl present in the pellet (estimated as 0.075 mg NaCl in a 20-μL pellet), V is the volume used for freeze-drying (4.5 mL) and m_{total} is the total mass of the PC-NP components (GNP-pre-crosslinked CS and TPP) in the batch, as expressed in Equation (4):

$$m_{total} = \frac{C_{CS} \times V_{CS} + C_{TPP} \times V_{TPP}}{V_{batch}} \quad (4)$$

where: C_{cs} is the concentration of CS in the GNP-pre-crosslinked CS gel (1 mg/mL), V_{cs} is the volume of the GNP-pre-crosslinked CS gel used for PC-NP preparation (4.125 mL or 3.750 mL in PC-A and PC-B, respectively), C_{TPP} is the concentration of the TPP solution (0.63 mg/mL), V_{TPP} is the volume of the TPP solution used for PC-NP preparation (1.875 mL or 2.250 mL in PC-A and PC-B, respectively) and V_{batch} is the total volume of the PC-NP batch (6 mL). Thus, m_{total} was estimated as 0.93 mg and 0.90 mg for PC-A and PC-B, respectively. PC-NP concentration was calculated during subsequent experimental steps (*e.g.*, isolation, dilution, etc) by applying the corresponding concentration factor, f_c (*i.e.*, volume of PC-NPs for isolation or dilution relative to batch volume), as follows (Equation (5)):

$$[NP](mg/mL) = m_{total} \times Production\ yield \times 10^{-2} \times f_c \quad (5)$$

Product yield determination was performed in triplicate.

2.6. Stability of PC-NPs in supplemented M9 minimal medium

60-μL aliquots of the isolated PC-NPs (PC-A and PC-B) were diluted in M9 minimal medium supplemented with 0.5% casamino acids, 1 mM thiamine hydrochloride and ampicillin (200 μg/mL), in a volume of 1 mL (final dilution = 1:17) and at a final concentration of ~ 0.15 mg/mL. The pH of the medium was 6.9 ± 0.05. The PC-NPs were incubated for 335 min in M9 minimal medium at 37 °C under shaking (100 rpm), and size variation was monitored every ten minutes by DLS-NIBS at 37 °C.

2.7. Bacterial strains and culture conditions

The *Escherichia coli* strain Top10 was transformed with plasmid pSB1A3-BBa_T9002, carrying the BBa_T9002 genetic device (Registry of Standard Biological Parts: http://parts.igem.org/Part:BBa_T9002), kindly donated by Prof. John C. Anderson (UC Berkeley, USA). The transformed strain is a biosensor that can respond to AHL [53]. Cultures were prepared as per the protocol described in our previous paper [42].

2.8. Evaluation of the ability of the PC-NPs to inhibit the QS response in a fluorescent E. coli biosensor of AHL-mediated QS

The QS inhibitory activity of the PC-NPs was evaluated in terms of their ability to decrease the AHL-mediated fluorescence response of the *E. coli* biosensor. Isolated PC-A and PC-B were serially diluted in water. Ten-μL aliquots of these dilutions were premixed with 180 μL of the biosensor's culture and incubated for one hour at 37 °C with shaking (100 rpm) in a flat-bottom, 96-well plate. Blank (medium only) and control wells were inoculated with 10 μL of water and incubated under the same conditions. After one hour, 10 μL of $5x10^{-9}$ M AHL were added to the wells to a final AHL concentration of $2.5x10^{-10}$ M and incubated for 300 min in the microplate reader as described (ref to IC-NPs). The final PC-NP concentration in the plate ranged from 0.1 to 0.001 mg/mL.

Statistical comparisons between PC-NP treatments and controls were made with GraphPad Prism version 6.00 (GraphPad Software, La Jolla California USA) using one-way ANOVA with multiple comparisons Dunnett's Test (** $p \leq 0.01$; *** $p \leq 0.001$; **** $p \leq 0.0001$). For each experiment, fluorescence intensity (FI) and optical density (OD_{600}) were corrected by subtracting the values of absorbance and fluorescence background and expressed as the average of three biological replicates. FI was normalized to cell density (FI/OD_{600}) [54].

2.9. Microscopy

Fluorescent imaging of the *E. coli* biosensor in the presence of AHL and PC-NPs was performed as follows. 180-μL aliquots of the biosensoŕs cultures were pre-incubated with 10-μL aliquots of PC-NPs, to a final NP concentration of 123 μg/mL for 40 min at 37 °C under shaking (100 rpm) in capped vials. The PC-NP pretreated biosensor was then induced with 10 μL of $5x10^{-9}$ M AHL. The cultures were then transferred to CytoCapture imaging dishes with 20-μm hexagonal cavities (Zell-Kontakt GmbH, Nörten-Hardenberg, Germany), and incubated for a further 60 min at room temperature before imaging by confocal laser scanning microscopy (CLSM). Images were recorded for a period of 70 min. Control cultures were prepared by adding equal aliquots of water instead of PC-NPs.

CLSM was performed using a Leica TCS SP2 spectral confocal scanner mounted on a Leica DM IRES inverted microscope. Images were acquired with the following settings: HCX PL APO 63.0x 1.20 W CORR UV water-immersion objective, argon excitation laser (488 nm), 134.1 μm pinhole (1.0 Airy unit), standard Leica settings for GFP beam path, emission bandwidth equal to 500–600 nm, and voxel width and height equal to 51.0 nm. Images were acquired from single scans with a line average of 4.0, scan speed of 400 Hz, and 8-bit resolution. Images were processed with Leica LAS AF Lite software with contrast and brightness values set to −63 and 0, respectively. To quantify fluorescence intensity data from representative CLSM images, a number of regions of interest (ROIs) were drawn as lines spanning the length of a representative number of cells (l = 1.9–4.3 μm) and used to measure pixel intensity across the cell. Every analysis included 3–7 images with 18–38 ROIs each. Three-dimensional analysis of the culture was performed by collecting z-series spanning a total thickness of 7–8 μm. A total of 22–27 frames were collected in each section, with 0.3-μm gaps between consecutive frames. Unpaired t-test comparisons between PC-NP treatments and controls were performed with GraphPad Prism version 6.00 (GraphPad Software, La Jolla California USA).

3. Results

3.1. Chemical co-crosslinking of CS with GNP

Prior to the fabrication of PC-NPs, pre-crosslinked CS/GNP mixtures with optimized composition and rheological properties were prepared in 85 mM NaCl after screening various GNP:CS mass ratios (see Materials and Methods). We and others have previously reported that moderate amounts of NaCl enhance the colloidal stability of TPP crosslinked CS NPs during their formation (see reference [42] for an extensive discussion on this issue). Fig. 1A shows representative images of GNP-pre-crosslinked CS at GNP:CS mass ratios of 0.06:1, 0.12:1 and 0.24:1 after 72 h incubation at 37C under shaking. Of note, the reaction between CS and GNP can be visually followed by the formation of a dark blue color, likely stemming from secondary products of the main reaction [13,15]. Both color intensity and the apparent loss in fluidity increased with increasing GNP:CS mass ratios [13]. At the highest GNP:CS mass ratio, a gel-like consistency was visually apparent (0.24:1 GNP:CS mass ratio in Fig. 1A). The crosslinking reaction between CS and GNP is well known, and its kinetics has been studied by UV, FTIR and ^{1}H NMR spectroscopy [14]. Here, we followed the kinetics of the crosslinking reaction by UV/VIS, DLS-NIBS and small deformation rheology. Fig. 1B shows the UV/VIS spectra (λ = 200–900 nm) depicting the time-course evolution of the GNP crosslinking reaction for CS/GNP mixtures with a GNP:CS mass ratio of 0.06:1. As previously reported, a characteristic peak between 280 and 300 nm (dotted line in Fig. 1B), increases concomitantly with the progression of the GNP crosslinking reaction [20]. The inset in Fig. 1B represents the evolution of the peak at 280 nm over time. The height of the peak increases steeply during the first 80 h of incubation and reaches a plateau at later times. This evidence made us conclude that the covalent crosslinking reaction was completed after 80 h. The DLS-NIBS intensity correlation data, obtained with different reaction times, were fitted to the KWW-based stretched exponential function (Eq. (1), see Materials and Methods), as previously described [45,51]. Fig. 1C shows the DLS-derived correlograms, expressed as correlation coefficients *vs.* delay times for a GNP:CS mass ratio of 0.06:1 and at different incubation times. The inset shows a representative correlogram of this GNP:CS mixture after 0.6 h incubation. The best-fit of the experimental data to the KWW-based stretched exponential function is represented by a solid line. Noticeable from Fig. 1C is the reduction in the magnitude of the intensity correlation coefficients at early delay times as incubation time increases. Fig. 1D plots the area under the curve (AUC) from the correlograms of Fig. 1C at different incubation times. A solid line depicts the monotonic decay of

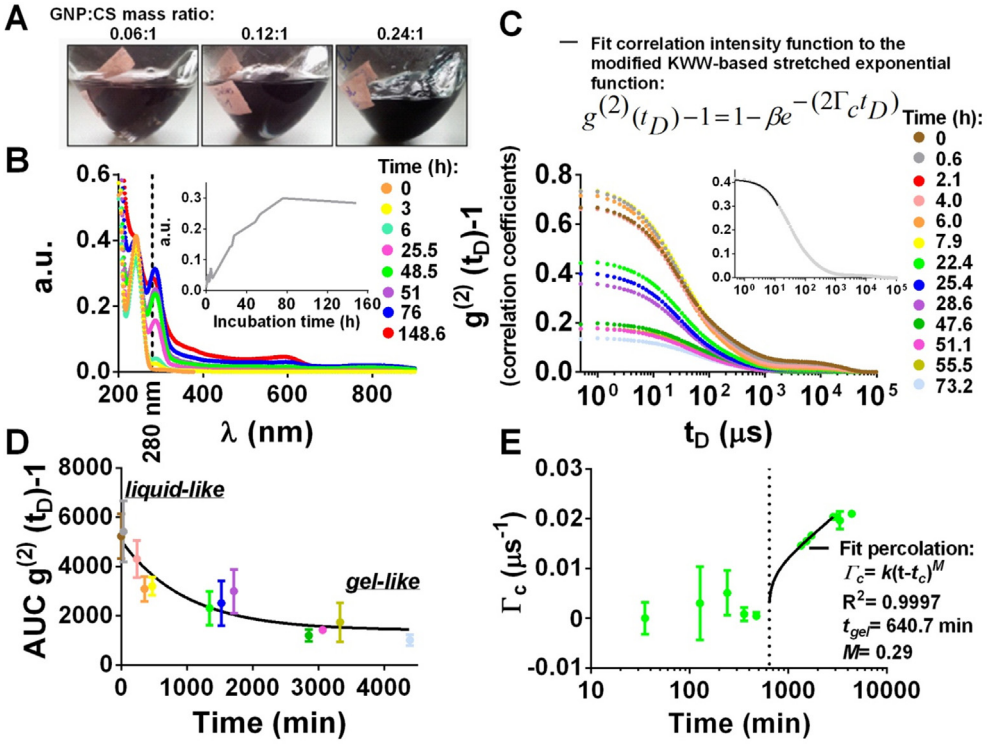

Fig. 1. Monitoring of chemical crosslinking of CS with GNP over time. A. Representative snapshots of the gelation-like process after incubation during 72 h at 37C with shaking. The images show the formation of blue color as a secondary product of the reaction of CS and GNP at different GNP:CS mass ratios; namely 0.06:1; 0.12:1 and 0.24:1. B. Time-course evolution of the crosslinking reaction for CS/GNP mixtures at a GNP:CS mass ratio of 0.06:1, as monitored by UV–vis scanning (λ = 200–900 nm). Color key indicates reaction times (right). The dotted line indicates the characteristic peak of the CS/GNP gelation reaction at λ = 280 nm. The inset shows the magnitude of the variation of the characteristic peak (λ = 280 nm) over time. Data corresponding to a single representative reaction. C. DLS-NIBS intensity correlograms at a GNP:CS mass ratio of 0.06:1. Color key indicates reaction times (right). The inset shows a representative plot at t = 73.2 h, where the solid black line represents the best-fit to the KWW-based stretched exponential function at early delay times. Data represent the mean of three technical replicates. For the sake of clarity, no error bars are shown. D. Evolution of the AUC from the plots in C with reaction time. Color-coded as in C. The solid line represents the best-fit of the data to the one-phase decay function (GraphPad Software, La Jolla California USA). Data represent the mean and standard deviations of three technical replicates. E. Evolution of the relaxation rate Γ_c, as estimated from the fits of the correlograms shown in C to the KWW-based function at different reaction times. The solid line corresponds to the best-fit of the data to the percolation function (Equation (2), see Materials and Methods). The dotted line indicates the estimated critical time of gelation ($t_{gel\text{-}DLS}$) at ~ 640.7 min. Data represent the mean and standard deviations of three technical replicates. (For interpretation of the references to color in this figure legend, the reader is referred to the web version of this article.)

the magnitude of AUC with incubation time in Fig. 1D. The strong decay in the initial amplitude of the correlation intensity, as depicted in Fig. 1D, has been proposed as a good indicator of the critical gelation time in previous studies with similar soft systems [45,55]. Fig. 1E shows a plot of the estimated Γ_c, as extracted from the fit shown in Fig. 1C, *vs.* time. The estimated values of Γ_c remained noisy around the baseline during the first ~ 35–500 min of incubation. After this phase, a sharp increase of estimated Γ_c values is observed ("take-off phase", from ~ 500–3000 min) that levels off late in the reaction ("plateau phase", after ~ 3000 min). This profile correlates closely with the one described by de Morais *et al.* [45] for the chemical crosslinking of CS with glutaraldehyde. As explained by these authors, the relaxation rate Γ_c, decreases at earlier reaction times due to an increase in viscous, hydrodynamic interactions between macromolecular CS coils and the solvent that result in longer macromolecular CS coils. At longer reaction times, further intermolecular crosslinking results in a decrease of the dimensions of the macromolecular coils in the gel structure and in loss of ergodicity, thus explaining the sharp Γ_c increase [45]. Upon closer inspection, the profile of estimated Γ_c *vs.* reaction time in Fig. 1E closely resembles the kinetics of a classical percolation process. The behavior of gels at the sol–gel phase transition has been extensively described in terms of Percolation Theory (PT) [44]. Percolative gelation involves a sharp transition at some intermediate critical point ($p = p_c$, Eq. (2); see Materials and Methods), where an infinite cluster starts to appear: a gel for p above p_c [44]. This critical point, or gel point, $p = p_c$ becomes $t = t_{gel\text{-}DLS}$ in our system and determines the critical gelation time (see Materials and Methods). We fitted the Γ_c values between the "take-off phase" and the "plateau phase" to the three-parameter power Belehradek function [47–48]. From this percolation fit, depicted by a solid line in Fig. 1E, a $t_{gel\text{-}DLS}$ of 640.7 min and an M exponent of 0.29, were obtained. The value of the M is not too far from the universal exponent reported for a 3D classical percolation process, M = 0.45 [44]. From these results, we can infer that a gel-like state is achieved after 10.7 h of incubation of the GNP-CS mixture at 37C and at a GNP:CS mass ratio of 0.06:1.

To further confirm the formation of a gel network, we examined the evolution of the viscoelastic properties during the sol–gel transition at a GNP:CS mass ratio of 0.06:1 by small deformation oscillatory rheology. The results (Fig. S1) revealed that an incipient gel network is formed at a rheological critical gel time ($t_{gel\text{-}rheo}$) of ~ 1118 min. This is evident from the crossover of the G' and G'' viscoelastic moduli, and the drop in the liquid-like character, tan δ (=G''/G'). Also, a frequency sweep recorded after 1200 min, revealed all the hallmarks of a gel network, namely $G' > G''$ *with little dependence of both moduli on* ω, the negative dependence of log η^* on log ω with a slope ~ −1.0 (Fig. S2). Despite being at the limit of sensitivity of the rheometer, these determinations provided unequivocal evidence of the sol–gel transition in the system. It should be noted, however, that the magnitude of the critical gel

time obtained by DLS-NIBS ($t_{gel\text{-}DLS}$ ~ 640.7 min) was ~ 2-fold lower than that determined by small deformation rheology ($t_{gel\text{-}rheo}$ ~ 1118 min). The apparent large discrepancy between the two determined values could be the result of the different experimental resolution capacity of each technique, as we have shown in a previous study at low CS concentrations (<2 mg/mL) [51]. Indeed, we have been able to show that within experimental error, DLS-NIBS, microviscosimetry and small deformation rheology constitute robust methods to determine the critical sol–gel transition of CS-based systems [51].

3.2. Optimization of PC-NP size and polydispersity

To obtain PC-NPs, the GNP-pre-crosslinked CS mixtures, formed as explained above, were further crosslinked with the ionic crosslinker TPP by following the classical ionotropic gelation protocol [6]. To rapidly assess the composition of PC-NPs with the lowest average NP diameter and PdI, we adopted the criteria described by Calvo *et al.* and Dmour & Taha [6,56]. Based on our previous and the work of others [5,42,57–59], we used 85 mM NaCl as a solvent instead of water to better modulate the size and the polydispersity of PC-NPs over a range of CS:TPP mass ratios. It has been suggested that the addition of a low amount of monovalent ions to CS NP suspensions aids in the optimization of the hydrodynamic radius and screens the electrostatic repulsion of the charged amino groups in CS, thus adopting a more compact conformation, increased flexibility and colloidal stability, and lower polydispersity [5,57].

Low Z-average hydrodynamic diameters and PdI values were attained with CS:TPP mass ratios in the range of 1.60:1 to 9.0:1 (See Materials and Methods and Table S1). The dependence of the size and PdI of PC-NPs on the relative TPP and CS concentrations is shown in Fig. 2A and 2B, respectively. In both cases, regions with colors ranging from green to red can be interpreted as hills with high size (Fig. 2A) or high PdI values (Fig. 2B), whereas regions with colors ranging from purple to blue correspond to valleys with sub-micron sizes and low-to-medium PdI values. Fig. 2A shows that it is possible to obtain PC-NPs with a Z-average diameter between ~ 200 and ~ 300 nm by using CS concentrations ranging from 0.5 to 1.5 mg/mL and TPP concentrations below 0.2 mg/mL. Close inspection of the contour plot also shows three conspicuous regions with sizes above ~ 600 nm, which correspond to specific compositions of CS and TPP, namely region 1, $\leq$ 0.9 mg/mL CS and $\geq$ 0.25 mg/mL TPP; region 2, 0.9–1.1 mg/mL CS and ~ 0.3–0.4 mg/mL TPP; and region 3, $\geq$ 1.1 mg/mL CS and > 0.3 mg/mL TPP (white dotted lines in Fig. 1A). Fig. 2B shows that low polydispersity was achieved in the PdI range of 0.2–0.3 for CS concentrations of 0.5–1.5 mg/mL and TPP concentrations below 0.2 mg/mL. Similarly to Fig. 2A, the contour plot in Fig. 2B displays two main regions of high polydispersity, PdI between ~ 0.5–1, which correspond to the following CS and TPP combinations: region 1, $\leq$ 0.7 mg/mL CS and $\geq$ 0.25 mg/mL TPP and region 2, ~ 0.7–1.1 mg/mL CS and > 0.35 mg/mL TPP (white dotted lines in Fig. 1B). Fig. 2C and 2D summarize the dependence of the size and PdI, respectively, on CS:TPP mass ratios. The Figures show that it was possible to obtain PC-NPs with an average diameter ranging from 100 to 250 nm and a low PdI values, ~ 0.1–0.2, under a wide range of CS:TPP mass ratios (2.6:1 to 9:1). PC-NPs could be easily dispersed in water, as has been reported for NPs prepared from CS of similar DA [60,61]. Two PC-NP prototypes displaying optimal size and PdI (indicated by black circles in Fig. 2C and 2D) were obtained with CS:TPP mass ratios of 3.5:1 and 2.6:1, respectively. These prototypes were designated as PC-A and PC-B and were selected for further studies.

The PC-A and PC-B prototype formulations were prepared by upscaling the PC-NP preparation method to 10-mL batches with a production yield of 44.5 and 40.9%, respectively (see Materials and Methods). The physicochemical characteristics of the PC-NP batches were analyzed by DLS-NIBS both before and after isolation (see Materials and Methods). Fig. 3 shows the polydispersity and the average diameter of PC-A (Fig. 3A) and PC-B (Fig. 3B), before and after isolation (cyan and orange plots, respectively). As shown in Fig. 3A, PC-A underwent a reduction in PdI after isolation, going from ~ 0.1 to ~ 0.04 (upper left y-axis). Yet, the average diameter remained stable (average diameter = 123.4 ± 6.6 nm and 124.0 ± 4.0 nm, for the non-isolated parent batch and the isolated batch, respectively). The bottom panels in Fig. 3A show a slight reduction in the width of the size distribution for isolated PC-NPs, relative to their parent batch. As shown in Fig. 3B, the parent batch of non-isolated PC-B is characterized by a lower PdI than that of PC-A, with a slight Pdl increase after isolation, namely from ~ 0.02 to ~ 0.04 (upper right y-axis). Parent PC-B NPs are, on the other hand, slightly larger than their PC-A counterparts, with an average diameter of 140.8 ± 3.2 nm before and 128.7 ± 2.5 nm after isolation. The bottom panels in Fig. 3B reveal no important differences between size distributions of parent and isolated PC-B batches. As expected, both PC-A and PC-B showed a marked positive ς-potential (~ +33 mV, data not shown), which is consistent with the presence of charged amine groups from CS exposed to the PC-NP surface [62,63].

3.3. PC-NP stability in M9 minimal medium

To evaluate the physical stability of PC-NPs designed for microbiological assays, we monitored particle size evolution during PC-NP incubation in our bioassay medium (see Materials and Methods). The chosen time range for these experiments, 335 min, was not arbitrary, as it spanned the duration of our typical bioassays with the *E. coli* biosensor (see below). Size and polydispersity plots in Fig. 4 revealed that both PC-A (Fig. 4A) and PC-B (Fig. 4B) remain fully stable during incubation in microbiological medium. The low PdI values between 0.06 and 0.1 confirmed that no aggregation or particle-growth took place during the incubation. Fig. 4C and 4D show that DLS-NIBS size distributions remained changeless over time in both cases.

3.4. Evaluation of the activity of PC-NPs using a fluorescence E coli biosensor

To analyze the QQ activity of PC-NPs, we used an *E. coli* biosensor that displays GFP fluorescence in response to external AHL [42,53]. When endpoint measurements are considered, both PC-A (Fig. 5A) and PC-B (Fig. 5B) promoted a significant reduction in the normalized fluorescence response of the biosensor, FI/OD_{600}. Comparison of Fig. 5A and 5B indicates that PC-B is slightly more active than PC-A, with relative reductions of endpoint FI/OD_{600} in the ranges of ~ 50–92% and ~ 35–85% of the control intensity, respectively. The endpoint measurements show the lack of a clear dose-dependent reduction of the response. Fig. 5C and 5D show the effect of PC-A and PC-B treatments on the growth rate of the *E. coli* biosensor (see also Fig. S3). Both PC-NP prototypes promote a significant reduction in growth rate that, much like the reduction in normalized fluorescence, is not proportional to the administered dose. Comparison of Fig. 5A and 5B to 5C and 5D shows that the magnitude of the growth impairment exerted by PC-NPs is much smaller than their effect on normalized fluorescence. Notably, CLSM imaging of the biosensor was consistent with the notion that the PC-NP-dependent decrease in fluorescence was much more accused than the antimicrobial effect (*cf.* Fig. S4A and B).

The plots shown in Fig. 5A-D fail to reveal the dynamics of the effect of PC-NPs on the growth and response of the biosensor. While we saw a significant degree of variation from experiment

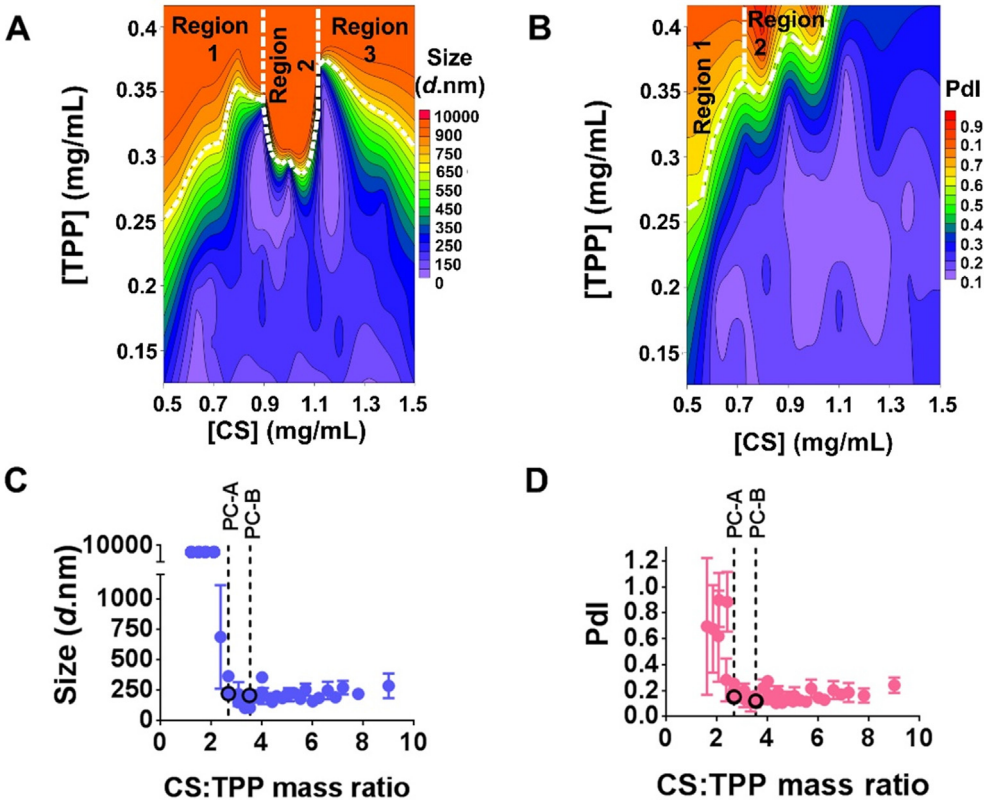

Fig. 2. Dependence of the size and PdI of PC-NPs on CS:TPP mass ratio. A and B. Contour plots showing the dependence of the size (A) and PdI (B) of PC-NPs on CS and TPP concentrations. [CS] = 0.5–1.5 mg/mL; [TPP] = 0.1–0.4 mg/mL; CS:GNP mass ratio = 1:0.06. White dotted lines in panels A and B show representative size and PdI regions (see text). C and D. Variation of PC-NP size (C) and polydispersity (D) as a function of the CS:TPP mass ratio. Dotted lines show the CS:TPP mass ratios 2.6:1 and 3.5:1, which correspond to the PC-NP prototypes PC-A and PC-B (black circles), respectively. Data represent the mean and standard deviation of three replicates. All measurements were conducted in water at 25 ± 0.2 °C.

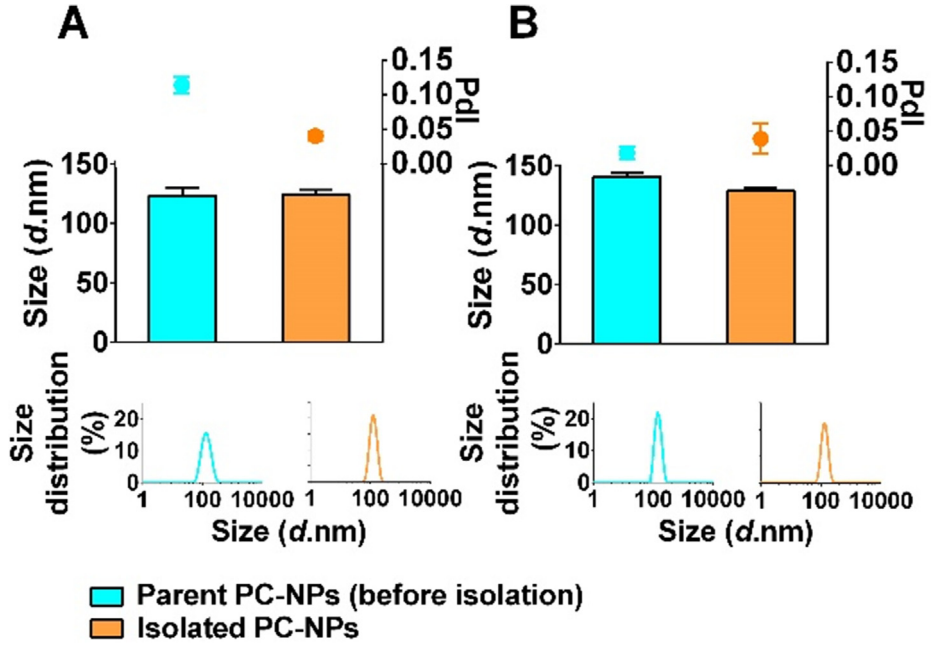

Fig. 3. Physico-chemical characterization of PC-NPs. A and B. Size and polydispersity of the parent batch before (cyan) and after (orange) isolation of PC-A (A) and PC-B (B) NPs. Bars represent mean size (left y-axis), whereas dots represent PdI values (upper right y-axis). Data represent the mean and standard deviation of three replicates. Bottom panels show representative DLS-NIBS size distribution plots for both PC-NP prototypes before and after isolation. All measurements were conducted in water at 25 ± 0.2 °C. (For interpretation of the references to color in this figure legend, the reader is referred to the web version of this article.)

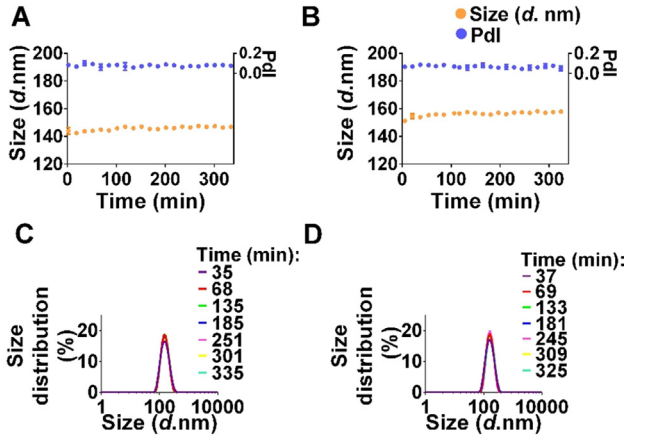

Fig. 4. Stability of PC-NPs in bioassay medium. A and B. Variation in size (orange dots; left y-axis) and in PdI values (blue dots; right y-axis) of PC-A (A) and PC-B (B) upon incubation at 37 °C in bioassay medium. Data represent the mean and standard deviation of three replicates. C and D. Representative DLS-NIBS size distributions of PC-A (A) and PC-B (B) at different times of incubation. All measurements were conducted in supplemented M9 minimal medium at 37 ± 0.1 °C. (For interpretation of the references to color in this figure legend, the reader is referred to the web version of this article.)

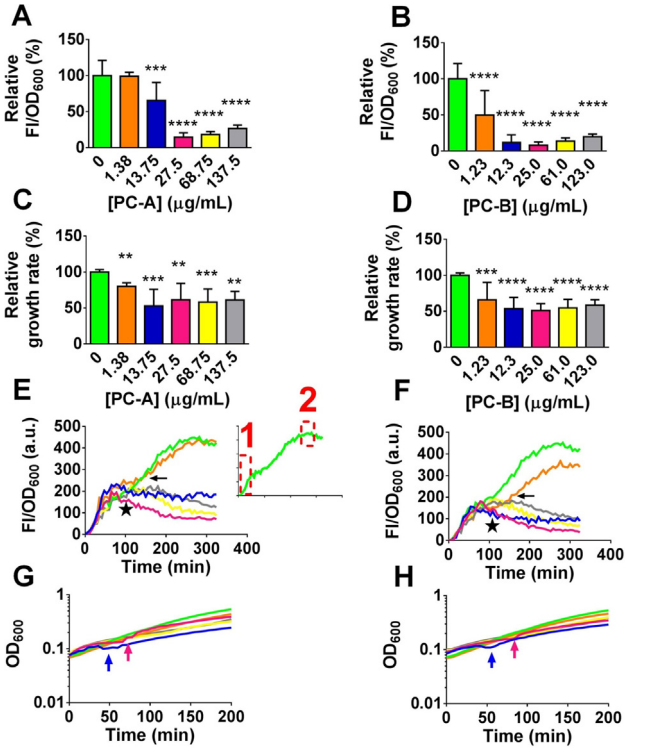

Fig. 5. Effect of PC-NPs on the QS-based fluorescent response and the growth of the *E. coli* biosensor. A and B. Endpoint FI/OD_{600} responses of the biosensor after treatment with various doses of PC-A (A) and PC-B (B) for 60 min prior to the addition of AHL. Data represent the mean and standard deviation of two independent experiments with three biological replicates each. P values are indicated as follows: **, $p \leq 0.01$; ***, $p \leq 0.001$; ****, $p \leq 0.0001$. C and D. Endpoint effect of PC-A (C) and PC-B (D) treatments on the bionsensor's growth rate. The mean and standard deviation of three independent experiments with three biological replicates each is shown. E and F. Representative FI/OD_{600} average traces of cultures treated with PC-A (E) and PC-B (F). The averages were obtained from a single experiment with three biological replicates. The traces are color coded as in A and B. For the sake of clarity, no error bars are shown (but see Figs. S1 and S2). Inset in panel E shows the typical biphasic response of non-treated cells. Box "1", initial burst of fluorescence. Box "2", fluorescence maximum. Arrowheads indicate the fluorescence recovery phases described in the text. Stars in panels E and F show the fluorescence dilution phase described in the text. G and H. Average growth curves for biosensor cells pre-treated with PC-A (G) and PC-B (H) prior to the addition of AHL. Arrowheads indicate the PC-NP-induced "shoulders" described in the text. The traces represent the mean of a single experiment with three biological replicates and are colour coded as in E and F. For the sake of clarity, no error bars are shown (but see Fig. S4). P values are indicated as follows: **, $p \leq 0.01$; ***, $p \leq 0.001$; ****, $p \leq 0.0001$.

to experiment, careful inspection of the average FI/OD_{600} traces (Fig. 5E and 5F, see also Figs. S5-S7), yields the following conclusions. First, in the absence of PC-NPs, the biosensor displays a biphasic response with a clear initial burst of fluorescence (see red-framed area "1″ in inset in Fig. 5E and also Fig. 5F, S5-S7). Following this initial burst, the control response steadily grows to reach a maximum of fluorescence at about ~ 250 min (see red-framed area "2" in the inset in Fig. 5E and also Fig. 5F, S5-S7). The burst was followed by a phase of fluorescence dilution at most of the PC-NP concentrations tested (black star in Fig. 5E and 5F). At low PC-NP concentrations, a recovery phase is sometimes visible (horizontal arrow in Fig. 5E and 5F, but see also Figs. S5-S7).

Fig. 5G and 5H show the average OD_{600} traces during the initial 200 min of incubation after AHL addition. Starting at a concentration of 13.75 μg/mL, incubation of the biosensor with PC-NPs resulted in curves displaying "shoulders" (arrows in Fig. 5G and 5H, Fig. 6). To better illustrate the nature of the PC-NP-induced "shoulders", in Fig. 6 we show the individual traces from all the three biological replicates, together with the average control trace. The boxes in Fig. 6 show that the "shoulders" observed in the average OD_{600} traces are related to the existence of PC-NP-dependent anomalies in the OD_{600} readings at certain times during growth (Fig. 6C-F see also Fig. S4). While there existed a significant degree of experiment-to-experiment variation regarding the magnitude of the anomalies in the growth kinetics of the PC-NP-treated cultures, the dose-dependence in the timing of the anomalies was very reproducible (Fig. 6; see also Fig. S5-S7). This dose dependence is more clearly illustrated in Fig. 7, which shows the relationship between the time of onset of OD_{600} anomalies and the concentration of PC-NPs. Strikingly, the data for both PC-A and PC-B can be easily fitted to hyperbolic curves, typical of dose–response relationships. The slightly steeper curve of PC-B is consistent with the higher inhibition of FI/OD_{600} displayed by these NPs in endpoint QQ measurements (cf. Fig. 5A and 5B). Of note, in the same assays, we also observed cell aggregates in the presence of the NPs (Fig. S8), in agreement with previous studies [42,64–65].

4. Discussion

We recently reported that TPP-crosslinked NPs (ionically crosslinked; IC-NPs) displayed substantial QQ activity despite their inherent colloidal instability in microbiological medium [42]. We also showed that additional GNP-crosslinking of IC-NPs resulted in more stable NPs (co-crosslinked; CC-NPs), albeit with a substantial loss of their QQ activity. This has motivated us to explore novel strategies to improve the physicochemical properties of IC-NPs while maintaining their QQ activity. In the present work, we addressed a new method for the fabrication of TPP-crosslinked NPs in which the pre-crosslinking of CS with GNP was followed by NP formation by conventional ionotropic gelation in the presence of TPP.

The most surprising aspect of the observed data of our study is that when the pre-gelled GNP/CS mix (GNP:CS mass ratio 0.06:1.0) was further ionotropically crosslinked by controlled addition of TPP (over a wide CS:TPP mass ratio of 2.6:1 to 9:1), the system turned into NPs of small conserved diameters (~100–150 nm) and low polydispersity (~0.1–0.2). To account for this phenomenon, we suggest the following. NP formation is the consequence of two separate physicochemical processes. Firstly, gelling by the creation of small nanoclusters resulting from the

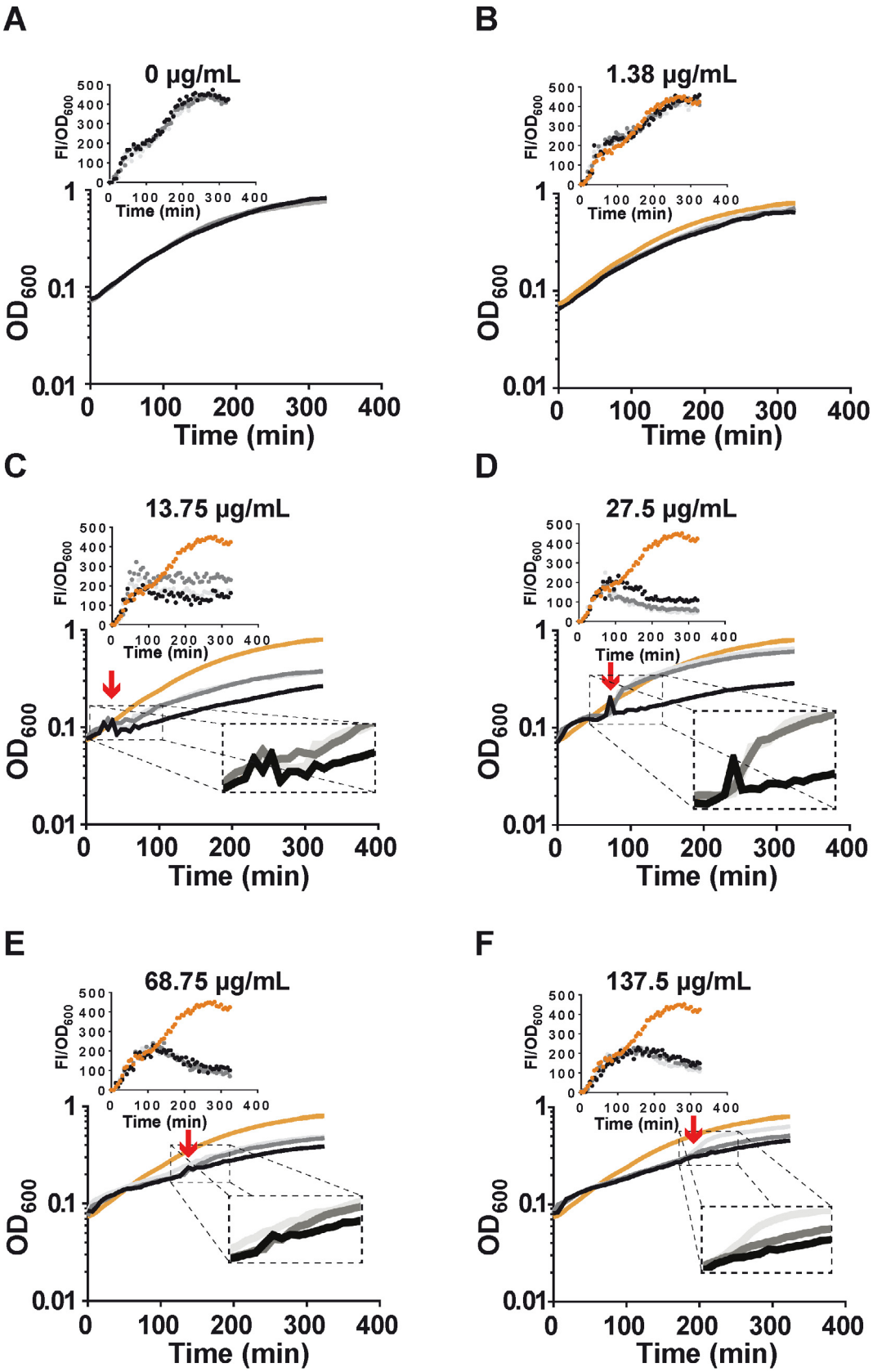

Fig. 6. Growth of the biosensor in the presence of increasing PC-A concentrations (A-F). The individual traces corresponding to the three replicates from a single experiment are shown with shades of gray. Orange traces: no NP controls. Boxes show enlarged views of the "shoulders". X axis: time in min. Y axis: OD_{600}. Insets show the corresponding plots of FI/OD_{600} *vs.* time for each treatment. (For interpretation of the references to color in this figure legend, the reader is referred to the web version of this article.)

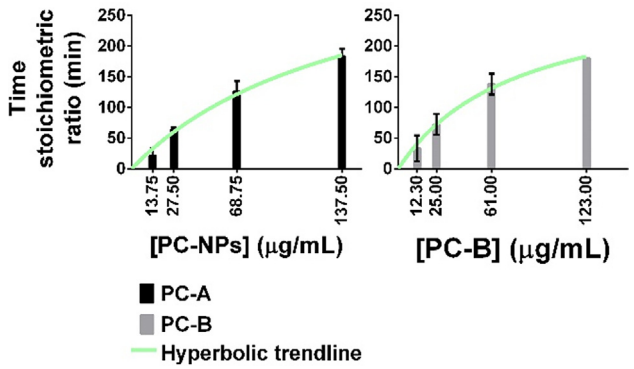

Fig. 7. Dose dependence of the OD_{600} anomalies. The time (in min) needed to reach the "shoulder region" at increasing PC-NP concentrations is shown for PC-A (black bars) and PC-B (gray bars). The times were estimated from visual examination of the OD_{600} *vs.* time plots shown in Figs. 6 and S2-4, considering that the "shoulder region" was reached once the individual traces diverged from one another (close-up boxes in Figs. 6 and S4-6). Data represent the mean and standard deviation of two independent experiments with three replicates each. The green line shows the approximation of the data to a hyperbolic curve (GraphPad Prism version 6.0). (For interpretation of the references to color in this figure legend, the reader is referred to the web version of this article.)

crosslinking of CS by GNP. Given the fact that the reaction was left to proceed to near equilibrium (72 h, Fig. 1D), we can regard the gelling process to be under thermodynamic control [51]. The entropic cost due to the loss of CS conformational mobility, as a result of the introduction of covalent "knots" between the polymer chains during the crosslinking process, is compensated by an overall gain in enthalpy from the formation of new chemical bonds and the favorable solvation of $-NH_3^+$ groups, preferentially oriented at the surface of the GNP-driven nanoclusters. As a result, a net decrease in surface free energy is obtained during gelling. Secondly, the addition of TPP to the incipiently gelled solution results in the shielding of the positively charged free amino groups in CS, leading to the condensation of the pre-gelled clusters into small discrete particles. The addition of TPP likely displaces the equilibrium and further contributes to the loss of polymer conformational mobility and the entropically unfavorable uneven partitioning of TPP within the CS-GNP pre-gelled clusters and the solvent. This could potentially drive the system into phase segregation of the clusters, as recently argued [51]. However, the vast entropy loss due to the tendency of a limiting amount of TPP ions to partition into the CS phase is counteracted by an overall reduction in particle size and, consequently, lower surface free energy, thus maintaining the system as a one-phase suspension. This overall hypothesis is consistent with results observed in CS-dextran sulfate nanocomplexes, where decreasing the kinetic control of the particle formation while favoring a thermodynamically (*i.e.,* equilibrium) controlled process is required to achieve NPs of high colloidal stability [66].

In summary, we assume that the process described here for the fabrication of CC-NPs leads to the formation of dense small colloidal particles stabilized by the presence of surface positive charges and by conformationally "frozen" polymer loops. Both features contribute concomitantly to electrostatic repulsion and steric stabilization of the system. A schematic view of the proposed model is shown in Fig. 8. Future biophysical studies such as TEM and AFM imaging, synchrotron SAXS, and asymmetric-flow field flow fractionation studies, will help deepen our understanding of the structure of these materials. Future work and microscopic imaging analysis should explore whether the two-step, raspberry-like organization of NPs described by Huang and Lapitsky [57] and proposed for the related CC-NPs [42] also applies to PC-NPs. On the same note, the possibility that PC-NPs may have a core–shell structure, as described for CC-NPs [42], should also be explored.

Even when the precise chemical mechanism at play during PC-NP synthesis remains to be fully elucidated, one practical implication of our method was to uncover a new fabrication protocol of physicochemically stable NPs. When compared to our previous fabrication method [42], our new strategy offers a simplified and highly reproducible procedure to obtain PC-NPs with a satisfactory yield and improved physicochemical properties such as size, ς-potential, and stability in biological medium (summarized in Table 1) [42]. The resulting PC-NPs had overall small diameter (~150 nm) and low PdI values (~0.1–0.3) from a wide range of relative CS:TPP mass ratios. GNP pre-crosslinking also makes the fabrication protocol much more straightforward and reliable. Crucially, the new protocol reduces the centrifugation steps used to isolate NPs from non-crosslinked CS [42,52,67]. As a result, the reproducibility of the fabrication method was greatly improved. We believe that the improved characteristics of PC-NPs, relative to related NPs [42], are likely due to a minimization of TPP induced aggregation [57,59].

The notable stability of PC-NPs in bacterial culture medium (pH 6.9) also coincides with that of core–shell CC-NPs, which also contain GNP and TPP but that underwent a different fabrication process, leading to distinct properties (see below) [42]. This stability, we argue, is the result of the combination of the covalent crosslinking and the ionotropic gelation used to fabricate these NPs as explained above. Altogether, the furnished PC-NPs (and CC-NPs) resist the tendency to disassemble and to inexorably aggregate that is observed with classical CS NPs (IC-NPs) in physiological media (pH ~ 7.0) [42,67]. Undoubtedly, to be stable in bacterial medium is a major asset of PC-NPs, also shared by CC-NPs [42].

We showed that PC-NPs display moderate antimicrobial activity, as judged by decreased OD_{600} readings, and strongly interfere with the QS-based fluorescence activity of the *E. coli* biosensor (Figs. 5 and 6). Since the fluorescence measurements have been normalized to cell density (FI/OD_{600}), the simple idea that the antimicrobial effect of our NPs might be responsible for the fluorescence decrease does not hold. On the contrary, the results show that the decrease in fluorescence was of greater magnitude than the OD_{600} drop caused by the antimicrobial effect. Preliminary CLSM trials confirmed the existence of a drastic decrease in per-cell fluorescence at the single-cell level (*cf.* Fig. S4A and S4B and Fig. S4C and S4D) that was not accompanied by a parallel reduction in cell numbers (Fig. S4E). This observation is in good agreement with the idea that the decreased OD_{600} values and reduced fluorescence are separate effects of PC-NP treatment. Indeed, it is even possible that the magnitude of the antimicrobial effect is an artifact caused by PC-NP-induced bacterial aggregation, as suggested earlier [42]. We have previously shown that the addition of CS NPs and nanocapsules (NCs) to bacterial cultures often results in growth anomalies such as those observed here (Fig. 6) [42,64]. In the case of CS NCs, we were able to show that only a limited number of NCs could electrostatically bind per bacterial cell, leading to the concept of the *stoichiometric ratio* (SR) of NC/bacterium [42,64]. At this NC/bacterium ratio, the negative ς-potential of the bacterial envelope is compensated by the positive charge of the NPs [64]. Increasing the NC concentration beyond the SR resulted in no further NP binding [64]. We have shown that the SR is accompanied by maximal, NC-induced cell aggregation [64]. We believe that the OD_{600} growth anomalies in the form of "shoulders", observed in the presence of intermediate concentrations of PC-NPs (Fig. 5G and 5H, Fig. 6, and Fig. S4-6), are likely related to cell aggregation and to the concept of SR, as described by Qin *et al.* [64]. Indeed, we have observed bacterial aggregation in the presence of PC-NPs (Fig. S8), further lending support to the hypothesis that our OD_{600} readings might not accurately reflect the actual cell density

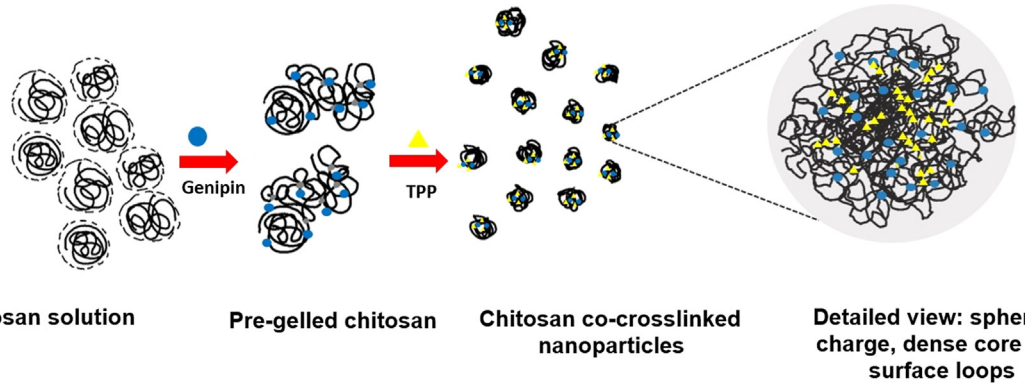

Fig. 8. Model of formation of PC-NPs showing the two steps of crosslinking with GNP and TPP and details of the structure and surface topology of the furnished NPs.

Table 1
Physico-chemical characteristics of our CS-NPs (this and our previous work [42].

	IC-NPs [42]	CC-NPs [42]	PC-NPs
Size in water (*d*. nm)	617 ± 232	151 ± 8	124 ± 4
Size in M9 medium(*) (*d*. nm)	N/A (&)	226 ± 19	147 ± 1
ξ (mV)	+25 ± 6	+20 ± 2	+33 ($)
PdI	0.1-0.2	0.1-0.2	0.03-0.05
Production yield (%)	40 ± 8 (!)	40 ± 8 (!)	50 ± 1
QQ activity	high	moderate	high
Antimicrobial activity	yes	yes	yes
Cell-density dependent activity	N/A	N/A	yes
Fabrication steps	2	4	3

(*) After 6 h incubation in M9 minimal medium at 37 °C.
(&) IC-NPs were unstable in M9 minimal medium at 37 °C, and there is no reliable DLS data available.
($) The measurement was performed only once.
(!) Production yield was estimated for the parent-non-isolated batch of IC-NPs before obtaining isolated IC- and CC-NPs.
Data, excepting ($) represent the mean and standard deviation of 3 (present work) to 9 replicates [42].

of the treated cultures. This interpretation would shed some light on the conspicuous lack of dose-dependence during PC-NP treatment of biosensor cells, that was already noted in our previous work [42], and that is clearly illustrated by the endpoint results of Fig. 5 [64]. Here, we have further investigated these growth anomalies by timing their onset at different NP concentrations. When this was done, dose dependence relative to NP concentration became apparent, as shown in Fig. 7. While we have observed relatively high levels of experimental variation (see Fig. 6 and Fig. S4-6), a trend is evident in which "shoulder" formation occurs at longer times as NP concentration increases. To explain this dose dependence at the onset of the growth anomalies, we will return to the SR concept. Since at constant NP concentrations, growing bacteria will find themselves at decreasing NP/bacterium ratios [64], we reasoned that PC-NP-induced aggregates produced at NP/bacterium ratios higher than the SR (early during growth) would be disrupted as these ratios became smaller than the SR. The dependence of the SR on cell density, together with its potential involvement in the appearance of OD_{600} anomalies, implies that the time at which a growing bacterial population encounters its SR must increase with NP concentration (*i.e.*, strictly, on the number of particles per unit volume). This prediction is fulfilled by the results of Fig. 7, which open up the possibility of targeting bacteria at different stages of growth by carefully tuning the concentration of PC-NPs to the desired bacterial density. For example, PC-NPs could be engineered for the precise release of bioactive molecules at a certain stage of bacterial growth. A full understanding of the role of cell aggregation in the appearance of the growth anomalies is required before this possibility can be developed into a new technological approach for density-dependent bacterial manipulation.

PC-NPs displayed a QQ activity that is comparable to those of the ionically crosslinked IC-NPs and raw CS preparations characterized earlier by our group (Table 1) [42,64–65]. Interestingly, the QQ activity of the dually crosslinked CC-NPs was much lower (Table 1), further attesting to the significance of the new fabrication method reported here. While the actual mechanism of QS inhibition has not been described for any of these CS-based materials, it is reasonable to think that a mode of action common to the three types of systems could explain their QQ activity. Using the PC-NPs described here as a representative example for all these materials, one could argue that NP binding to the bacterial envelope may affect the uptake of nutrients and, as a result, the apparent QQ activity would merely be the consequence of a general metabolic impairment. As discussed above, the reduced OD_{600} values obtained in the presence of PC-NPs might not reflect decreased growth, at least not to the levels suggested by the plots of Fig. 5. Strikingly, the initial slope of the burst in the fluorescence response curve (first 100 min after induction with AHL) obtained in the presence of PC-NPs is not different from those obtained in the absence of NPs. This is despite the fact that treated cells had been pre-incubated with PC-NPs for an hour before induction (see Fig. 5E-F and insets of Fig. S4-6). This observation is in clear disagreement with the idea that metabolic arrest was the main cause of the observed PC-NP-induced, endpoint reduction in FI/OD_{600}, as one would expect to see slower fluorescence accumulation immediately after AHL induction in metabolically arrested cells. In an alternative QQ mechanism, NPs could act as "chemical abductors", by sequestering AHL from the medium. However, the absence of dose-dependence associated with the QQ activity displayed by PC-NPs is in clear disagreement with their potential "AHL abducting" ability. This very lack of dose dependence, especially during the initial burst phase, also rules out a simple mechanism in which the coating of the external envelope with CS-NPs made the cells impermeable to AHLs. Perhaps the explanation of the QQ activity of PC-NPs might have to do with the direct perturbation of the QS machinery of the biosensor by the binding of CS-NPs to the bacterial envelope [64,68–70]. Kolibachuck and Greenberg published in 1993 a report in which they described LuxR as a membrane-associated protein in its native *Vibrio fischeri* host [71]. This result was later confirmed for other related QS activators [71,72]. Considering these observations, the idea that a potential interference of

envelope-bound, CS-based NPs with the membrane localization of LuxR could provide a reasonable explanation to our results. Despite the intrinsic appeal of this hypothesis, many issues remain to be elucidated, not the least of which is whether LuxR membrane localization holds true in the *E. coli* biosensor. Finally, while this and our previous work [42] demonstrate the QQ potential of CS-based NPs, it remains to be seen whether this potential is applicable only to luxR-based systems or, by the contrary, if it could be expanded to other types of QS networks. Testing the QQ activity of both PC-NPs and CC-NPs against bacterial pathogenic Gram-positive strains such as *Staphylococcus aureus* [73] and *Streptococcus mutants* [74], for which QS is known to be regulated by signaling peptides and membrane-associated receptors, could be considered in future studies. The possibility to inhibit biofilm formation in these type of bacteria could hold great promise. Also, CS-based NPs could bear an enormous potential as biodegradable, antibiotic-free and antibacterial strategies that can be used against pathogenic multidrug resistant pathogens such as *Staphylococcus aureus*, *Pseudomonas aeruginosa*, *Klebsiella pneumonia,* among other [76,77].

5. Conclusions

Here, we present a simplified and robust method to fabricate CS NPs by covalent crosslinking of CS with GNP close to the critical gelling condition, followed by the formation of CS NPs by ionic gelation with TPP. This new approach enables to obtain NPs with improved physico-chemical properties and physiological colloidal stability, and display strong QQ activities. Their mode of action, we hypothesise that is consistent with the existence of a SR of NP/bacterium, at which the negative ς-potential potential of the bacterial envelope is counteracted by the positive charge of the NPs. The fact that the establishment of this SR displays clear dose dependence on bacterial density, implies that these NPs could be ideal for applications in which the targeting of bacterial populations at specific cell densities is desired. This work represents an improved strategy over the previously reported methods to manipulate CS into small NPs [6] by combining the colloidal stability of co-crosslinked NPs with the QS inhibition activity of IC-NPs [42]. We believe that the QQ capacity of CS-based NPs deserves further attention as part of the search for novel anti-QS strategies that can be used to counteract the growth of bacterial pathogens in the context of the spread of antimicrobial resistance. This work also expands the available strategies for the design of nanomaterials with the capacity to carry and deliver bioactive molecules.

CRediT authorship contribution statement

C. Vila-Sanjurjo: Conceptualization, Methodology, Investigation, Writing - original draft. **L. Hembach:** Methodology, Investigation. **J. Netzer:** Investigation. **C. Remuñán-López:** Supervision, Writing - review & editing. **A. Vila-Sanjurjo:** Supervision, Conceptualization, Writing - review & editing. **F.M. Goycoolea:** Conceptualization, Writing - review & editing, Supervision.

Declaration of Competing Interest

The authors declare that they have no known competing financial interests or personal relationships that could have appeared to influence the work reported in this paper.

Acknowledgments

This work was supported by the FP7 IIF Marie Curie project entitled BioNanoSmart_DDS (Contract No. 221111), and by funds for the Consolidation and Structuration of Competitive Research Units (Competitive Reference Groups) (REF. 2010/18), from the Spain Institute of Health "Carlos III" (Strategic Health Action, Project FIS PSI14/00059) and Xunta de Galicia (Project Competitive Reference Groups, ED431C 2017/09-FEDER and ED431C 2018/57). CVS was supported by a pre-doctoral fellowship of the Xunta de Galicia (Spain) and by a FPU fellowship of the Ministerio de Educación y Ciencia (Spain), by a research fellowship of the DAAD (Germany), and a research fellowship of the Fundación Pedro Barrié de la Maza (Spain). We thank Christopher Anderson and Mariana Leguia for providing plasmid pSB1A3-BBa_T9002, Carlos Bustamante for his support during the optimization of the *E. coli* fluorescent biosensor. We are also grateful to Antje von Schaewen for the generous access to the Safire Tecan-F129013 Microplate Reader.

Appendix A. Supplementary data

Supplementary data to this article can be found online at https://doi.org/10.1016/j.jcis.2020.05.075.

References

[1] M. Rinaudo, Chitin and Chitosan: Properties and Applications, Prog. Polym. Sci. 31 (7) (2006) 603–632.
[2] M. Dash, F. Chiellini, R.M. Ottenbrite, E. Chiellini, Chitosan—A Versatile Semi-Synthetic Polymer in Biomedical Applications, Prog. Polym. Sci. 36 (8) (2011) 981–1014.
[3] J. Berger, M. Reist, J.M. Mayer, O. Felt, N.A. Peppas, R. Gurny, Structure and Interactions in Covalently and Ionically Crosslinked Chitosan Hydrogels for Biomedical Applications, Eur. J. Pharm. Biopharm. 57 (1) (2004) 19–34.
[4] M.J. Moura, H. Faneca, M.P. Lima, M.H. Gil, M.M. Figueiredo, In Situ Forming Chitosan Hydrogels Prepared via Ionic/Covalent Co-Cross-Linking, Biomacromolecules 12 (9) (2011) 3275–3284.
[5] H. Jonassen, A.L. Kjøniksen, M. Hiorth, Effects of Ionic Strength on the Size and Compactness of Chitosan Nanoparticles, Colloid Polym. Sci. 290 (10) (2012) 919–929.
[6] P. Calvo, C. Remunan-Lopez, J. Vila-Jato, M.J. Alonso, Novel Hydrophilic Chitosan-Polyethylene Oxide Nanoparticles as Protein Carriers, J. Appl. Polym. Sci. 63 (1997) 125–132.
[7] H. Liu, C. Gao, Preparation and Properties of Ionically Cross-Linked Chitosan Nanoparticles, Polym. Adv. Technol. 20 (7) (2009) 613–619.
[8] X. Zhang, S. Malhotra, M. Molina, R. Haag, Micro- and Nanogels with Labile Crosslinks - from Synthesis to Biomedical Applications, Chem. Soc. Rev. 44 (7) (2015) 1948–1973.
[9] Y. Kawashima, T. Handa, A. Kasai, H. Takenaka, S.Y. Lin, Y. Ando, Novel Method for the Preparation of Controlled-Release Theophylline Granules Coated with a Polyelectrolyte Complex of Sodium Polyphosphate-Chitosan, J. Pharm. Sci. 74 (3) (1985) 264–268.
[10] T.K. Giri, A. Thakur, A. Alexander, H. Badwaik, D.K. Tripathi, Modified Chitosan Hydrogels as Drug Delivery and Tissue Engineering Systems: Present Status and Applications, Acta Pharm. Sin. B 2 (5) (2012) 439–449.
[11] Y.-H. Lin, S.-C. Tsai, C.-H. Lai, C.-H. Lee, Z.S. He, G.-C. Tseng, Genipin-Cross-Linked Fucose-Chitosan/Heparin Nanoparticles for the Eradication of Helicobacter Pylori, Biomaterials 34 (18) (2013) 4466–4479.
[12] Y. Zhang, Y. Thomas, E. Kim, G.F. Payne, PH- and Voltage-Responsive Chitosan Hydrogel through Covalent Cross-Linking with Catechol, J. Phys. Chem. B 116 (5) (2012) 1579–1585.
[13] B.M. Espinosa-García, W.M. Argüelles-Monal, J. Hernández, L. Félix-Valenzuela, N. Acosta, F.M. Goycoolea, Molecularly Imprinted Chitosan-Genipin Hydrogels with Recognition Capacity toward o-Xylene, Biomacromolecules 8 (2007) 3355–3364.
[14] M.F. Butler, Y.-F. Ng, P.D.A. Pudney, Mechanism and Kinetics of the Crosslinking Reaction between Biopolymers Containing Primary Amine Groups and Genipin, J. Polym. Sci. Part A Polym. Chem. 41 (24) (2003) 3941–3953.
[15] F.L. Mi, H.W. Sung, S.S. Shyu, Synthesis and Characterization of a Novel Chitosan-Based Network Prepared Using Naturally Occurring Crosslinker, J. Polym. Sci. Part A Polym. Chem. 38 (15) (2000) 2804–2814.
[16] R.A.A. Muzzarelli, Genipin-Crosslinked Chitosan Hydrogels as Biomedical and Pharmaceutical Aids, Carbohydr. Polym. 77 (1) (2009) 1–9.
[17] Y. Yuan, B.M. Chesnutt, G. Utturkar, W.O. Haggard, Y. Yang, J.L. Ong, J.D. Bumgardner, The Effect of Cross-Linking of Chitosan Microspheres with Genipin on Protein Release, Carbohydr. Polym. 68 (3) (2007) 561–567.
[18] M.P. Klein, C.R. Hackenhaar, A.S.G. Lorenzoni, R.C. Rodrigues, T.M.H. Costa, J.L. Ninow, P.F. Hertz, Chitosan Crosslinked with Genipin as Support Matrix for Application in Food Process: Support Characterization and β-d-Galactosidase Immobilization, Carbohydr. Polym. 137 (2016) 184–190.

[19] X. Song, H. Wu, S. Li, Y. Wang, X. Ma, M. Tan, Ultrasmall Chitosan-Genipin Nanocarriers Fabricated from Reverse Microemulsion Process for Tumor Photothermal Therapy in Mice, Biomacromolecules 16 (7) (2015) 2080–2090.
[20] R. Harris, E. Lecumberri, A. Heras, Chitosan-Genipin Microspheres for the Controlled Release of Drugs: Clarithromycin, Tramadol and Heparin. Mar., Drugs 8 (6) (2010) 1750–1762.
[21] Hongmei Chen, Wei Ouyang, Christopher Martoni, Satya Prakash, Genipin Cross-Linked Polymeric Alginate-Chitosan Microcapsules for Oral Delivery: In-Vitro Analysis, Int. J. Polym. Sc. 2009 (2009).
[22] B.L. Bassler, R. Losick, Bacterially Speaking, Cell 125 (2) (2006) 237–246.
[23] S.T. Rutherford, B.L. Bassler, Bacterial Quorum Sensing: Its Role in Virulence and Possibilities for Its Control, Cold Spring Harb. Perspect. Med. 2 (11) (2012) a012427.
[24] W.L. Ng, B.L. Bassler, Bacterial Quorum-Sensing Network Architectures, Ann. Rev. Genet. 43 (2009) 197–222.
[25] M.E. Taga, B.L. Bassler, Chemical Communication among Bacteria, Proc. Natl. Acad. Sci. U. S. A. 100 (2) (2003) 14549–14554.
[26] M.E.A. Churchill, L. Chen, Structural Basis of Acyl-Homoserine Lactone-Dependent Signaling, Chem. Rev. 111 (1) (2011) 68–85.
[27] C. Fuqua, E.P. Greenberg, Listening in on Bacteria: Acyl-Homoserine Lactone Signalling, Nat. Rev. Mol. Cell Biol. 3 (9) (2002) 685–695.
[28] B. Koch, T. Liljefors, T. Persson, J. Nielsen, S. Kjelleberg, M. Givskov, The LuxR Receptor: The Sites of Interaction with Quorum-Sensing Signals and Inhibitors, Microbiology 151 (11) (2005) 3589–3602.
[29] N. Qin, S.M. Callahan, P.V. Dunlap, A.M. Stevens, Analysis of LuxR Regulon Gene Expression during Quorum Sensing in Vibrio Fischeri, J. Bacteriol. 189 (11) (2007) 4127–4134.
[30] B. LaSarre, M.J. Federle, Exploiting Quorum Sensing To Confuse Bacterial Pathogens, Microbiol. Mol. Biol. Rev. 77 (1) (2013) 73–111.
[31] J.E. Gonzalez, N.D. Keshavan, Messing with Bacterial Quorum Sensing, Microbiol. Mol. Biol. Rev. 70 (4) (2006) 859–875.
[32] Q.H. Christensen, T.L. Grove, S.J. Booker, E.P. Greenberg, A High-Throughput Screen for Quorum-Sensing Inhibitors That Target Acyl-Homoserine Lactone Synthases, Proc. Natl. Acad. Sci. U. S. A. 110 (34) (2013) 13815–13820.
[33] M. Romero, L. Acuña, A. Otero, Patents on Quorum Quenching: Interfering with Bacterial Communication as a Strategy to Fight Infections, Recent Pat. Biotechnol. 6 (1) (2012) 2–12.
[34] M. Manefield, T.B. Rasmussen, M. Henzter, J.B. Andersen, P. Steinberg, S. Kjelleberg, M. Givskov, Halogenated Furanones Inhibit Quorum Sensing through Accelerated LuxR Turnover, Microbiology 148 (Pt 4) (2002) 1119–1127.
[35] C. Mayer, M. Romero, A. Muras, A. Otero, Aii20J, a Wide-Spectrum Thermostable N-Acylhomoserine Lactonase from the Marine Bacterium Tenacibaculum Sp. 20J, Can Quench AHL-Mediated Acid Resistance in Escherichia Coli, Appl. Microbiol. Biotechnol. 99 (22) (2015) 9523–9539.
[36] E.V. Piletska, G. Stavroulakis, L.D. Larcombe, M.J. Whitcombe, A. Sharma, S. Primrose, G.K. Robinson, S.A. Piletsky, Passive Control of Quorum Sensing: Prevention of Pseudomonas Aeruginosa Biofilm Formation by Imprinted Polymers, Biomacromolecules 12 (4) (2011) 1067–1071.
[37] E. Cavaleiro, I. Chianella, M.J. Whitcombe, S.A. Piletsky, A. Correia, A.S. Duarte, Synthetic Polymers Capable of Suppressing Virulence of Bacterial Fish Pathogens, Curr. Opin. Biotechnol. 22 (2011) S79.
[38] A.M. Piras, G. Maisetta, S. Sandreschi, M. Gazzarri, C. Bartoli, L. Grassi, S. Esin, F. Chiellini, G. Batoni, Chitosan Nanoparticles Loaded with the Antimicrobial Peptide Temporin B Exert a Long-Term Antibacterial Activity in Vitro against Clinical Isolates of Staphylococcus Epidermidis, Front. Microbiol. 6 (2015) 372.
[39] A. Gupta, J.L. Terrell, R. Fernandes, M.B. Dowling, G.F. Payne, S.R. Raghavan, W. E. Bentley, Encapsulated Fusion Protein Confers “Sense and Respond” Activity to Chitosan-Alginate Capsules to Manipulate Bacterial Quorum Sensing, Biotechnol. Bioeng. 110 (2) (2013) 552–562.
[40] L. Cobrado, M.M. Azevedo, A. Silva-Dias, J.P. Ramos, C. Pina-Vaz, A.G. Rodrigues, Cerium, Chitosan and Hamamelitannin as Novel Biofilm Inhibitors?, J. Antimicrob. Chemother. 67 (5) (2012) 1159–1162.
[41] E.M. Costa, S. Silva, C. Pina, F.K. Tavaria, M. Pintado, Antimicrobial Effect of Chitosan against Periodontal Pathogens Biofilms, SOJ. Microbiol. Infect. Dis. 2 (1) (2014) 1–6.
[42] C. Vila-Sanjurjo, L. David, C. Remuñán-López, A. Vila-Sanjurjo, F.M. Goycoolea, Effect of the Ultrastructure of Chitosan Nanoparticles in Colloidal Stability, Quorum Quenching and Antibacterial Activities, J. Colloid Interface Sci. 556 (2019) 592–605, https://doi.org/10.1016/j.jcis.2019.08.061.
[43] K. Tanaka, K. Nishida, B. Gabrys, J. Lawrence, M. Kanaya, Critical Dissolution Ionic Strength of Aqueous Solution of Chitosan Hydrochloride Salt, Sen-i Gakkaishi J. Soc. Fiber Sci. Technol. Japan 70 (2014) 225–231.
[44] D. Stauffer, A. Coniglio, M. Adam Gelation and Critical Phenomena. In Polymer Networks; Dušek, K., Ed.; Springer Berlin Heidelberg: Berlin, Heidelberg, 1982, pp 103–158.
[45] W.A. de Morais, M.R. Pereira, J.L.C. Fonseca, Characterization of Gelification of Chitosan Solutions by Dynamic Light Scattering, Carbohydr. Polym. 87 (4) (2012) 2376–2380.
[46] D. Stauffer, A. Aharony, Cluster Numbers, in: D. Stauffer, A. Aharony (Eds.), Introduction to Percolation Theory, UK Taylor & Francis Ltd., London, 1994, pp. 15–59.
[47] T. Sauerwald, J. Hennemann, C.-D. Kohl, T. Wagner, S. Russ, H2S Detection Utilizing Percolation Effects in Copper Oxide, Proc Sens 2013 (2013) 656–660.
[48] K. Kurselis, R. Kiyan, V.N. Bagratashvili, V.K. Popov, B.N. Chichkov, 3D Fabrication of All-Polymer Conductive Microstructures by Two Photon Polymerization, Opt. Express 21 (25) (2013) 31029–31035.
[49] C. Vila-Sanjurjo, C. Engwer, X. Qin, L. Hembach, T. Verdía-Cotelo, C. Remuñán-López, A. Vila-Sanjurjo, F.M. Goycoolea, A Single Intracellular Protein Governs the Critical Transition from an Individual to a Coordinated Population Response during Quorum Sensing: Origins of Primordial Language, bioRxiv (2016).
[50] C.-Y.M. Tung, P.J. Dynes, Relationship between Viscoelastic Properties and Gelation in Thermosetting Systems, J. Appl. Polym. Sci. 27 (2) (1982) 569–574.
[51] C. Engwer, R. Loy, I.S. Chronakis, C. Mendes, M. Francisco, Mesoscopic Gelation of Chitosan and Genipin at below Critical Concentrations, ChemRxiv (2017) 1–10, https://doi.org/10.26434/chemrxiv.5487172.v1.
[52] E.L.S. Carvalho, A. Grenha, C. Remuñán-López, M.J. Alonso, B. Seijo, Mucosal Delivery of Liposome-Chitosan Nanoparticle Complexes, Methods Enzymol. 465 (2009) 289–312.
[53] B. Canton, A. Labno, D. Endy, Refinement and Standardization of Synthetic Biological Parts and Devices, Nat. Biotechnol. 26 (7) (2008) 787–793.
[54] A. Oslizlo, P. Stefanic, I. Dogsa, I. Mandic-Mulec, Private Link between Signal and Response in Bacillus Subtilis Quorum Sensing, Proc. Natl. Acad. Sci. U. S. A. 111 (4) (2014) 1586–1591.
[55] M. Shibayama, Universality and Specificity of Polymer Gels Viewed by Scattering Methods, Bull. Chem. Soc. Jpn. 79 (12) (2006) 1799–1819.
[56] I. Dmour, M.O. Taha, Novel Nanoparticles Based on Chitosan-Dicarboxylate Conjugates via Tandem Ionotropic/Covalent Crosslinking with Tripolyphosphate and Subsequent Evaluation as Drug Delivery Vehicles, Int. J. Pharm. 529 (1–2) (2017) 15–31.
[57] Y. Huang, Y. Lapitsky, Salt-Assisted Mechanistic Analysis of Chitosan/Tripolyphosphate Micro- and Nanogel Formation, Biomacromolecules 13 (11) (2012) 3868–3876.
[58] Y. Huang, Y. Lapitsky, Monovalent Salt Enhances Colloidal Stability during the Formation of Chitosan/Tripolyphosphate Microgels, Langmuir 27 (17) (2011) 10392–10399.
[59] Y. Huang, Y. Lapitsky, On the Kinetics of Chitosan/Tripolyphosphate Micro- and Nanogel Aggregation and Their Effects on Particle Polydispersity, J. Colloid Interface Sci. 486 (2017) 27–37.
[60] H.-C. Yang, M.-H. Hon, The Effect of the Degree of Deacetylation of Chitosan Nanoparticles and Its Characterization and Encapsulation Efficiency on Drug Delivery, Polym. Plast. Technol. Eng. 49 (12) (2010) 1292–1296.
[61] S. Sreekumar, F.M. Goycoolea, B.M. Moerschbacher, G.R. Rivera-Rodriguez, Parameters Influencing the Size of Chitosan-TPP Nano- and Microparticles, Sci. Rep. 8 (1) (2018) 4695.
[62] M.A. Razi, R. Wakabayashi, Y. Tahara, M. Goto, N. Kamiya, Genipin-Stabilized Caseinate-Chitosan Nanoparticles for Enhanced Stability and Anti-Cancer Activity of Curcumin, Colloids Surf. B Biointerf. 164 (2018) 308–315.
[63] M.A. Mohammed, J.T.M. Syeda, K.M. Wasan, E.K. Wasan, An Overview of Chitosan Nanoparticles and Its Application in Non-Parenteral Drug Delivery, Pharmaceutics 9 (2017) (4), https://doi.org/10.3390/pharmaceutics9040053.
[64] X. Qin, C. Engwer, S. Desai, C. Vila-Sanjurjo, F.M. Goycoolea, An Investigation of the Interactions between an E. Coli Bacterial Quorum Sensing Biosensor and Chitosan-Based Nanocapsules, Colloids Surf. B Biointerf. 149 (2017) 358–368.
[65] X. Qin, J. Emich, F. Goycoolea, Assessment of the Quorum Sensing Inhibition Activity of a Non-Toxic Chitosan in an N-Acyl Homoserine Lactone (AHL)-Based Escherichia Coli Biosensor, Biomolecules 8 (3) (2018) 87.
[66] M. Costalat, L. David, T. Delair, Reversible Controlled Assembly of Chitosan and Dextran Sulfate: A New Method for Nanoparticle Elaboration, Carbohydr. Polym. 102 (1) (2014) 717–726.
[67] M.J. Masarudin, S.M. Cutts, B.J. Evison, D.R. Phillips, P.J. Pigram, Factors Determining the Stability, Size Distribution, and Cellular Accumulation of Small, Monodisperse Chitosan Nanoparticles as Candidate Vectors for Anticancer Drug Delivery: Application to the Passive Encapsulation of [14C]-Doxorubicin, Nanotechnol. Sci. Appl. 8 (2015) 67.
[68] I. Helander, E.-L. Nurmiaho-Lassila, R. Ahvenainen, J. Rhoades, S. Roller, Chitosan Disrupts the Barrier Properties of the Outer Membrane of Gram-Negative Bacteria, Int. J. Food Microbiol. 71 (2–3) (2001) 235–244.
[69] S.J. Jeon, M. Oh, W.-S. Yeo, K.N. Galvão, K.C. Jeong, Underlying Mechanism of Antimicrobial Activity of Chitosan Microparticles and Implications for the Treatment of Infectious Diseases, PLoS One 9 (3) (2014) e92723.
[70] M.M. Fernandes, A. Francesko, J. Torrent-Burgués, F.J. Carrión-Fité, T. Heinze, T. Tzanov, Sonochemically Processed Cationic Nanocapsules: Efficient Antimicrobials with Membrane Disturbing Capacity, Biomacromolecules 15 (4) (2014) 1365–1374.
[71] D. Kolibachuk, E.P. Greenberg, The Vibrio Fischeri Luminescence Gene Activator LuxR Is a Membrane-Associated Protein, J. Bacteriol. 175 (22) (1993) 7307–7312.
[72] Y. Qin, Z.-Q. Luo, A.J. Smyth, P. Gao, S. Beck von Bodman, S.K. Farrand, Quorum-Sensing Signal Binding Results in Dimerization of TraR and Its Release from Membranes into the Cytoplasm, EMBO J. 19 (19) (2000) 5212–5221, https://doi.org/10.1093/emboj/19.19.5212.
[73] M. Thoendel, A.R. Horswill, Identification of Staphylococcus Aureus AgrD Residues Required for Autoinducing Peptide Biosynthesis, J. Biol. Chem. 284 (33) (2009) 21828–21838.
[74] G. Kaur, P. Balamurugan, S. Adline Princy Inhibition of the Quorum Sensing System (ComDE Pathway) by Aromatic 1,3-Di-m-Tolylurea (DMTU): Cariostatic Effect with Fluoride in Wistar Rats. Front. Cell. Infect. Microbiol. 2017, 7 313.